

Revealing Short-period Exoplanets and Brown Dwarfs in the Galactic Bulge using the Microlensing Xallarap Effect with the *Nancy Grace Roman Space Telescope*

SHOTA MIYAZAKI^{†,1}, SAMSON A. JOHNSON,² TAKAHIRO SUMI,¹ MATTHEW T. PENNY,³ NAOKI KOSHIMOTO,⁴ AND
TSUBASA YAMAWAKI¹

¹*Department of Earth and Space Science, Graduate School of Science, Osaka University, 1-1 Machikaneyama, Toyonaka, Osaka 560-0043, Japan*

²*Department of Astronomy, The Ohio State University, 140 West 18th Avenue, Columbus OH 43210, USA*

³*Department of Physics and Astronomy, Louisiana State University, Baton Rouge, LA 70803, USA*

⁴*Department of Astronomy, Graduate School of Science, The University of Tokyo, 7-3-1 Hongo, Bunkyo-ku, Tokyo 113-0033, Japan*

(Revised January 4, 2022)

ABSTRACT

The *Nancy Grace Roman Space Telescope* (*Roman*) will provide an enormous number of microlensing light curves with much better photometric precisions than ongoing ground-based observations. Such light curves will enable us to observe high-order microlensing effects which have been previously difficult to detect. In this paper, we investigate *Roman*'s potential to detect and characterize short-period planets and brown dwarfs (BDs) in source systems using the orbital motion of source stars, the so-called xallarap effect. We analytically estimate the measurement uncertainties of xallarap parameters using Fisher matrix analysis. We show that the *Roman* Galactic Exoplanet Survey (RGES) can detect warm Jupiters with masses down to $0.5 M_{\text{Jup}}$ and orbital periods of 30 days via the xallarap effect. Assuming a planetary frequency function from Cumming et al. (2008), we find *Roman* will detect ~ 10 hot and warm Jupiters and ~ 30 close-in BDs around microlensed source stars during the microlensing survey. These detections are likely to be accompanied by the measurements of the companion's masses and orbital elements, which will aid in the study of the physical properties for close-in planet and BD populations in the Galactic bulge.

Keywords: Exoplanets (498), Hot Jupiters (753), Brown dwarfs (185), Galactic bulge (2041), Gravitational microlensing (672), Xallarap effect (2139)

1. INTRODUCTION

Gravitational microlensing (Mao & Paczynski 1991; Bennett & Rhie 1996) has a unique sensitivity to low-mass exoplanets beyond the snow line (Hayashi et al. 1985) where planet formation is considered active by the enhanced surface density of solid materials. It has maximum sensitivity to planets (around the lens objects) with projected semi-major axes roughly equal to the projected Einstein ring radius R_E , where

$$R_E = \left(\frac{4GM_L}{c^2} \frac{D_L D_{LS}}{D_S} \right)^{1/2}. \quad (1)$$

Here D_S and D_L are the distances of the source and lens from the Earth, M_L is the mass of the lens, and

$D_{LS} = D_S - D_L$. For typical microlensing events toward the Galactic bulge ($D_S = 8$ kpc, $D_L = 4$ kpc, $M_L = 0.3 M_\odot$), R_E is ~ 2.3 au. Using this “binary-lens” channel of microlensing, the *Nancy Grace Roman Space Telescope* (Spergel et al. 2015, previously named *WFIRST*, hereafter *Roman*) will conduct the *Roman* Galactic Exoplanet Survey and discover ~ 1400 cold wide-orbit exoplanets (Penny et al. 2019, hereafter P19) and provide an otherwise-inaccessible statistical sample of exoplanets in previously un-probed regions of exoplanet parameter space (see Figure 9 of P19).

Roman will detect many thousands of microlensing light curves which will generally have better photometric precision than many ground-based microlensing surveys. This will enable the measurement of high-order microlensing effects which have been previously difficult to detect. One of the high-order effects that can be mea-

surable in the *Roman* light curves is xallarap (Griest & Hu 1992; Han & Gould 1997; Poindexter et al. 2005). Xallarap is a microlensing effect where the reflex motion of a source star in a binary system modulates the magnification of the source star. A more commonly known microlensing effect, orbital microlens parallax (Gould 2004), also causes the variations with the same mechanism by the orbital motion of an observer.¹ The xallarap amplitude ξ_E corresponds to the semi-major axis of the source star a_S normalized by the angular Einstein radius θ_E projected to the source plane, i.e.,

$$\xi_E = \frac{a_S}{D_S \theta_E} = \frac{a_S}{\hat{r}_E}, \quad (2)$$

where \hat{r}_E is the projected Einstein radii. We note that a_S is the distance between the source and the center of masses of the source system. Using Newton's version of Kepler's third law, we can derive following equations from the Equation (2),

$$\begin{aligned} \xi_E &= \frac{1 \text{ au}}{\hat{r}_E} \left(\frac{M_P}{M_\odot} \right) \left[\frac{M_\odot}{M_S + M_P} \frac{P_\xi}{1 \text{ yr}} \right]^{2/3} \\ &\simeq 2 \times 10^{-5} \left(\frac{1 \text{ au}}{D_S \theta_E} \right) \left(\frac{M_P}{M_{\text{Jup}}} \right) \left[\frac{M_\odot}{M_S + M_P} \frac{P_\xi}{1 \text{ day}} \right]^{2/3} \end{aligned} \quad (3)$$

$$M_S a_S = M_P a_P$$

$$\Rightarrow a \equiv a_S + a_P = \left(1 + \frac{M_S}{M_P} \right) a_S, \quad (4)$$

where M_S and M_P are masses of the source (host) and source companion, P_ξ is the orbital period, a_P is the semi-major axis of the source companion, and a is the distance between the host and companion in the source system.

Equation (3) means that when a solar-type source star in the Galactic bulge ($D_S = 8 \text{ kpc}$) is accompanied by a planet with $M_P = 10 M_{\text{Jup}}$ and $P_\xi = 10 \text{ days}$, the angular size of the semi-major axis of the source star orbit around the barycenter is a factor 10^{-4} smaller than θ_E . Present ground-based microlensing survey observations do not have typical sensitivities to detect such small fluctuations induced by planetary-mass source companions.

In several microlensing analyses, xallarap has been investigated to explain light curve deviations from a standard model (Paczynski 1986) which assumes uniform linear motions between the source, lens, and observers (e.g. Bennett et al. 2008; Sumi et al. 2016). However, identifying the xallarap signals clearly is rarely successful. For example, Sumi et al. (2010) analyzed a planetary microlensing event OGLE-2007-BLG-368 and found clear

asymmetric features that can be interpreted as xallarap signals. However, they could not conclude it because possible unknown systematics in the light curve could not be ruled out. Recently, Miyazaki et al. (2020) identified a significant xallarap signal in a planetary microlensing event OGLE-2013-BLG-0911. Using the observed xallarap parameters, they concluded that there is a late M-dwarf orbiting the source star with a mass of $0.14^{+0.02}_{-0.02} M_\odot$ and an orbital period of $36.7^{+0.8}_{-0.7} \text{ days}$. This is the first demonstration that dark, low-mass objects in the Galactic bulge can be detected and characterized via xallarap even with ground-based photometry. Rahvar & Dominik (2009) suggested a possibility that planets orbiting sources in the Galactic bulge are detectable via xallarap with sufficiently good photometry. With space-based photometry like *Roman*, planetary-mass objects might be detectable and characterizable via xallarap.

In this paper, we investigate the possibility of detecting planetary xallarap signals in the *Roman* microlensing events. In Section 2, we describe our Fisher matrix analysis and analytical quantification of the ability of the *Roman* light curves to detect xallarap signals and characterize the physical properties of the source systems. To predict how many planets are detectable in the *Roman* mission via the xallarap effect, we apply our analysis to simulations of the *Roman* survey in Section 3. Finally, we give our conclusion and discussion in Section 4.

2. FISHER MATRIX ANALYSIS

In this section, we conduct the Fisher matrix analysis based on the expected *Roman* observations and evaluate its sensitivity for xallarap. Rahvar & Dominik (2009) adopted the value of $\Delta\chi^2$ between the xallarap and non-xallarap (standard) models as the detection threshold of the source companion. However, it could be insufficient for evaluating the ability to characterize the physical parameters of planets. Further discussion on this is presented in Appendix A. The mechanisms of how xallarap affects light curves are essentially identical to the microlens parallax. Therefore, we conduct the Fisher matrix analysis by modifying the formulas of parallax that are conducted by Gould (2013), Mogavero et al. (2016, hereafter M16), and Bachelet et al. (2018, hereafter B18).

2.1. Parameterization of the Xallarap effect

Here we describe the xallarap effect observed by a single observatory. We follow B18's descriptions for the parallax effect observed by space-based observatories and then modify it for the case of xallarap effect.

¹ Xallarap can be considered as the inverse of parallax and is a semordnilap.

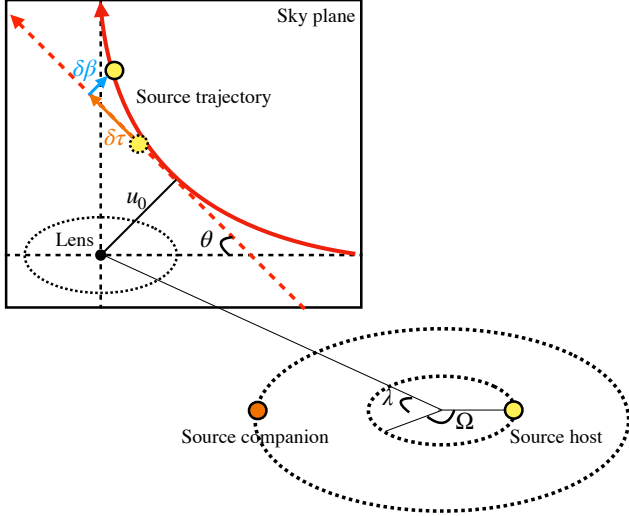


Figure 1. Schematic view of the xallarap problem. Due to the source orbital motion, the source trajectory (solid red curve) deviates from the inertial trajectory (dashed red line).

In general, the observed flux of microlensing event is

$$F = F_S A + F_B = \bar{F} [(1 - \nu)A + \nu] \quad (5)$$

where F_S , F_B , $\bar{F} (\equiv F_S + F_B)$ are the fluxes of the source, blend and baseline, respectively. $\nu \equiv F_B / (F_S + F_B)$ denotes the blend flux ratio². For a single-lens single-source (1L1S) model, the source flux magnification A is described by

$$A(t) = \frac{u^2(t) + 2}{u(t)\sqrt{u^2(t) + 4}}, \quad (6)$$

where u is the magnitude of the lens-source separation vector normalized by the angular Einstein radius θ_E , \mathbf{u} . For uniform linear motions between the source, lens, and observers, $u(t) = \sqrt{\tau^2 + u_0^2}$, where $\tau \equiv (t - t_0)/t_E$, t_0 is the time of the magnification peak, and u_0 is the lens-source impact parameter normalized to θ_E .

Figure 1 gives a schematic view of the xallarap problem. Here we consider a planet in a circular orbit ($e = 0$) around a source star with orbital period P_ξ and mass M_P . Then the source also orbits around the barycenter of the source system. In this paper, we assume that the source companion contributes no flux to the event, i.e. it acts as a 1L1S event, not a binary source event (Han & Jeong 1998). The displacement of the source position due to the orbital motion can be described by

$$\mathbf{S}(t) = \begin{pmatrix} s_1 \\ s_2 \end{pmatrix} = \begin{pmatrix} \cos \Omega - \cos \phi_\xi \\ \sin \lambda_\xi (\sin \Omega - \sin \phi_\xi) \end{pmatrix}, \quad (7)$$

² \bar{F} and ν are non-standard variables.

where $\Omega = \omega(t - t_0) + \phi_\xi$ and $\omega = 2\pi/P_\xi$. Here, λ_ξ denotes the inclination of the source orbital plane with respect to the observer and ϕ_ξ denotes the orbital phase at t_0 . We define θ as the angle between the direction of the lens-source relative motion and the major axis of the source orbit projected on the sky. When we define the xallarap vector $\boldsymbol{\xi}_E = (\xi_{E,\parallel}, \xi_{E,\perp}) = \xi_E(\cos \theta, \sin \theta)$, the displacement of the source position due to the orbit relative to the inertial source position is

$$\delta\tau = \boldsymbol{\xi}_E \cdot \mathbf{S} \quad (8)$$

$$\delta\beta = \boldsymbol{\xi}_E \times \mathbf{S}, \quad (9)$$

where $|\boldsymbol{\xi}_E| = a_S / (D_S \theta_E)$. The lens-source separation vector $\mathbf{u}(t)$ can be described by

$$\mathbf{u}(t) = \begin{pmatrix} \tau' \cos \theta - u' \sin \theta \\ \tau' \sin \theta + u' \cos \theta \end{pmatrix}, \quad (10)$$

where $\tau' = \tau + \delta\tau$ and $u' = u_0 + \delta\beta$. The xallarap model can be described by ten parameters:

$$\boldsymbol{\zeta} = (\bar{F}, \nu, t_0, t_E, u_0, \xi_{E,\parallel}, \xi_{E,\perp}, \phi_\xi, \lambda_\xi, P_\xi). \quad (11)$$

2.2. Fisher Matrix Analysis

To estimate the expected uncertainty of each parameter (ζ_i) by the *Roman* microlensing survey, we calculate the Fisher matrix of the light curve model $F(t_k, \boldsymbol{\zeta})$ with given parameter set $\boldsymbol{\zeta}$. Under the assumption of independent errors, the Fisher matrix elements $b_{i,j}$ can be written as

$$b_{i,j} = \sum_{k=1}^N \frac{1}{\sigma_k^2} \frac{\partial F(t_k)}{\partial \zeta_i} \frac{\partial F(t_k)}{\partial \zeta_j} \quad (12)$$

where N is the total number of the data points, and σ_k is the photometric error on data point at t_k . Once the Fisher matrix is calculated, the covariance matrix for parameters \mathbf{C} is given by its inverse matrix, i.e.,

$$\mathbf{C} = \mathbf{b}^{-1}. \quad (13)$$

We follow the logic of M16 and discard (negligible) contribution of \bar{F} from our Fisher matrix analysis³. In principle, the uncertainties for the xallarap amplitude depend on the event geometry, i.e., $\sigma_{\xi_E}^2(\theta, \phi_\xi)$. To produce the results which are independent from the geometric conditions, M16 analytically found the minimum

³ An arbitrary uncertainty on \bar{F} is achievable with a sufficient number of photometric observations while the event is at baseline. *Roman* will collect $\sim 40,000$ measurements in its *W146* bandpass per light curve during the survey, which spans 6×72 -d seasons spread out over 4.5 years.

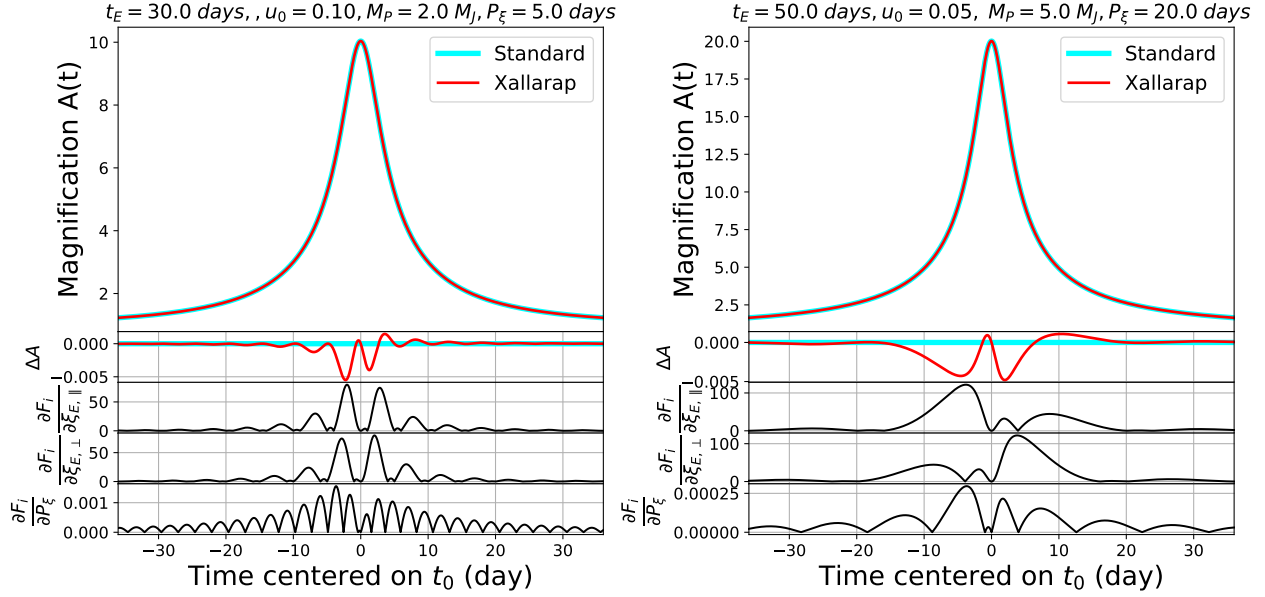


Figure 2. Two examples of simulated *Roman* light curves with xallarap. Top: The standard (cyan solid line) and xallarap (solid red line) light curves. Second to the Top: The residuals of the xallarap light curves relative to the standard ones. The three bottom panels: The absolute values of components of integrands of the Fisher matrix $\partial F(t_k)/\partial \zeta_i$ at a given time t_k .

uncertainty on parallax measurement, $\sigma_{\pi_E, \min}^2$, which is independent of θ . We modify it for xallarap measurements $\sigma_{\xi_E, \min}^2(\phi_\xi)$ as

$$\sigma_{\xi_E, \pm}^2(\phi_\xi) = \frac{\sigma_{\xi_E, \parallel}^2 + \sigma_{\xi_E, \perp}^2}{2} \pm \frac{\sqrt{(\sigma_{\xi_E, \parallel}^2 - \sigma_{\xi_E, \perp}^2)^2 + 4\text{cov}(\xi_{E, \parallel}, \xi_{E, \perp})^2}}{2},$$

$$\sigma_{\xi_E, \min}^2 \equiv \min_{\phi_\xi \in [0, 2\pi]} \sigma_{\xi_E, -}^2(\phi_\xi). \quad (14)$$

As M16 noted, for $P_\xi \ll u_0 t_E$, the covariance between the xallarap vector components $\xi_{E, \parallel}$ and $\xi_{E, \perp}$ disappear so that σ_{ξ_E} becomes independent of ϕ_ξ .

In this work, we assume continuous observations of 72 days with a 15 min cadence and Gaussian photometric errors that are consistent with simulated photometric error bars shown in Figure 4 of P19. Periodic correlated noise is expected to be mainly produced by spacecraft systematics and stellar pressure-driven (*p*-mode) oscillations. Detailed photometric simulations on all systematic errors are computationally expensive. P19 applied sub-optimal aperture photometry in their simulated photometric pipeline and added a Gaussian systematic error floor of 1 mmag in quadrature into their photometric results to compensate for un-modeled systematic errors. Timescales of xallarap signals, which are typically > 0.1 day, are much longer than the expected timescale of *p*-mode oscillations of main-sequence stars (Broomhall et al. 2009). Moreover, Gilliland et al. (2015) found that most *Kepler* stars have a median

photometric variability of ~ 0.2 mmag, with timescale of < 0.6 hr. This is somewhat smaller than P19's error floor of 1 mmag.

We also assume the source mass and distance to be $M_S = 1 M_\odot$ and $D_S = 8$ kpc, respectively, and the angular Einstein radius to be $\theta_E = 0.3$ mas, which approximately leads to

$$\xi_E \sim 4.6 \times 10^{-5} \left(\frac{M_P}{M_{\text{Jup}}} \right) \left(\frac{P_\xi}{\text{day}} \right)^{2/3}. \quad (15)$$

In our analysis, we consider the orbital inclination of $\lambda_\xi = 45^\circ$ and t_0 to be at center of 72 days *Roman* observing window. Our result is hardly dependent on θ because we adopt $\sigma_{\xi_E, \min}$ that is independent of the event geometry. Here we set $\theta = 45^\circ$. For each *W146S*, we adopt the value of the blend flux ratio ν to be the same with the median value of the ν distribution that is obtained by the P19 simulation. Note that we assume the microlens parallax effect does not affect the measurement of xallarap effect because the xallarap period we focus here is much shorter than 365 days for the parallax, and is thus likely distinguishable. We do not consider the finite source effect (Witt & Mao 1994) because the effect can be easily modeled and is distinguishable from xallarap. We also do not consider binary-lens events. Although the binary-lens event would be more sensitive to the xallarap effect than the single-lens event, it is outside the scope of this work. We also ignore any accelerations induced by *Roman*'s orbit around L2.

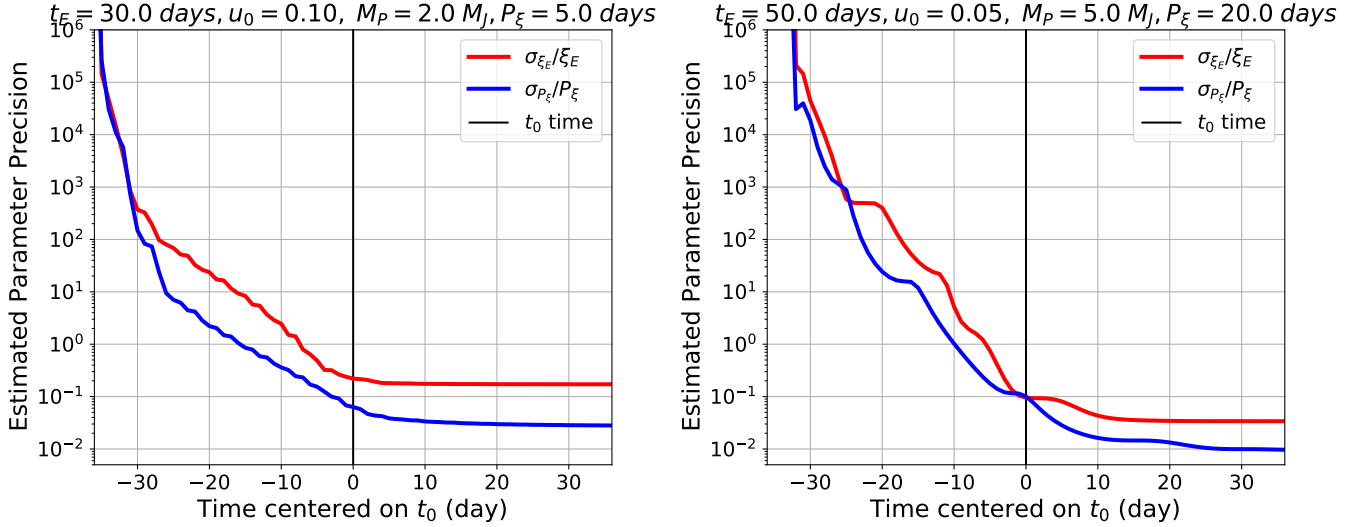


Figure 3. Parameter uncertainties for the xallarap amplitude ξ_E (red lines) and orbital period P_E (blue lines) estimated at each time when a *Roman* observation is conducted. To obtain these lines, we calculate the covariance matrices from the Fisher matrix at each observation. The parameter conditions for the two panels are identical to that of Figure 2.

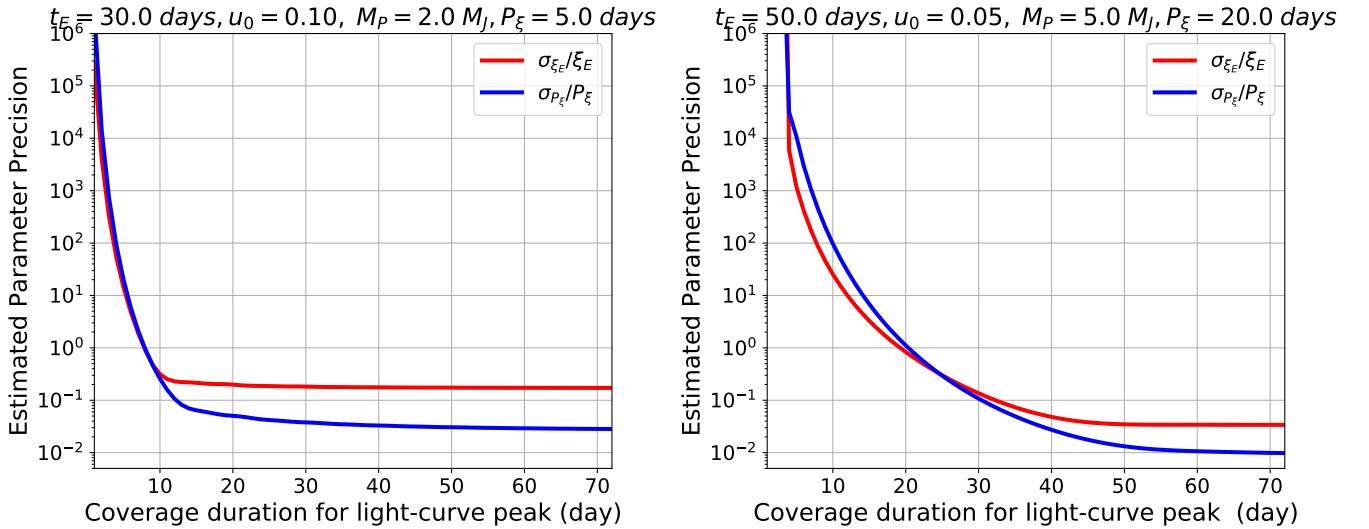


Figure 4. Parameter uncertainties for the xallarap amplitude ξ_E (red lines) and orbital period P_E (blue lines) as a function of the coverage duration for the light-curve peak (t_0). For plotting these, data points of *Roman* light curve are uniformly distributed within the duration centered on t_0 and then we conduct the Fisher matrix analysis using the data points. The parameter conditions for the two panels are identical to that of Figure 2.

The nominal expected fractional error on the companion mass can be derived from Equation (3) as

$$\frac{\sigma_{M_P}}{M_P} = \sqrt{\left(\frac{\sigma_{\xi_E, \min}}{\xi_E}\right)^2 + \frac{4}{9} \left(\frac{\sigma_{P_E}}{P_E}\right)^2}, \quad (16)$$

by assuming the uncertainties on θ_E , D_S , and M_S are negligible. We set the detection threshold for the xallarap companions as $(\sigma_{M_P}/M_P) = 0.3$ in the following analysis. The impacts of uncertainties of θ_E , D_S , and M_S on the measurements of companion's masses is discussed in Appendix B.

2.3. Xallarap Light Curves

Figure 2 shows two samples of model light curves with and without xallarap effect in the top panels. The residuals of light curves between that with xallarap and without are shown in the second panels. The left figure represents an event with $t_E = 30$ days, $u_0 = 0.1$, $M_P = 2 M_{\text{Jup}}$ and $P_E = 5$ days. In this case, the maximum deviations from the standard model is about 0.5% of the source flux, which is comparable to the *Roman* photometric noise level for $W146 \sim 20$ mag (see Figure

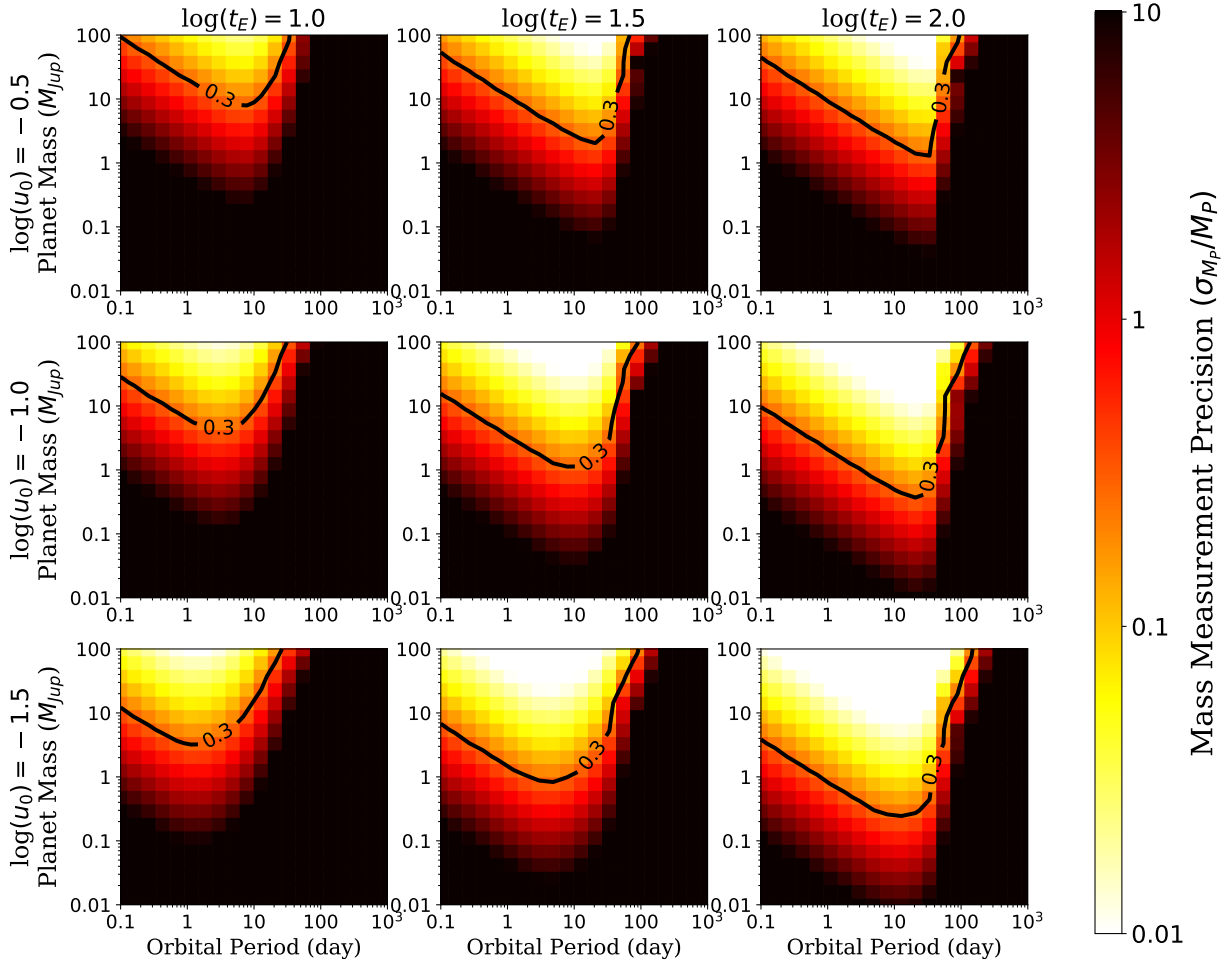


Figure 5. Color map distributions of the planetary mass error $\left(\frac{\sigma_{M_P}}{M_P}\right)$ for an event with the source magnitude of $W146_S = 18$ mag.

4 of P19). This indicates that brighter and/or high-magnification events are promising targets for *Roman* to detect xallarap features induced by a Jupiter-mass planet around the source star. In the three bottom panels, we plot the components of integrands of the Fisher matrix $\partial F(t_k)/\partial \zeta_i$ at a given time t_k . These panels imply that the observations during $t_0 \pm P_\xi$ are most important to determine the xallarap parameters (ζ_i) related to the mass of companion M_P . However, note that observations further into the wings continue to add to the precision of the period estimate (see the most bottom panels).

For understanding what parts of light curves are important to constrain the parameters, we derive the parameter uncertainties using the Fisher matrix analysis at each time when a *Roman* observation is conducted. Figure 3 represents the cumulative precisions on ξ_E and P_ξ as a function of time for the *Roman* light curve with $W146_S = 18$ mag (corresponding to Figure 2). We found that the parameter uncertainties are gradu-

ally constrained with increasing data points from the wing of the light curves. Moreover, we also derive the cumulative precision on the parameters as a function of the coverage duration for the light curve peak (Figure 4). We found that the resultant parameter precisions strongly depend on how long the light curves cover around the event peaks. Figure 3 and 4 indicate that the xallarap parameters can be measured with incomplete light curves that cover around $t_0 \pm P_\xi$. This is particularly important for *Roman*, which has a short observing window of 72 days.

2.4. Xallarap Sensitivity Map

At a given $(t_E, u_0, W146_S)$, we conducted the Fisher matrix analysis on a grid of points over the ranges of $-2 \leq \log(M_P/M_{\text{Jup}}) \leq 2$ and $-1 \leq \log(P_\xi/\text{day}) \leq 3$ with 20×20 grid points, respectively. In Figure 5, we present samples of xallarap sensitivity maps in the mass-orbital period plane for the *Roman* event with $W146_S = 18$ mag. The color maps in each panel rep-

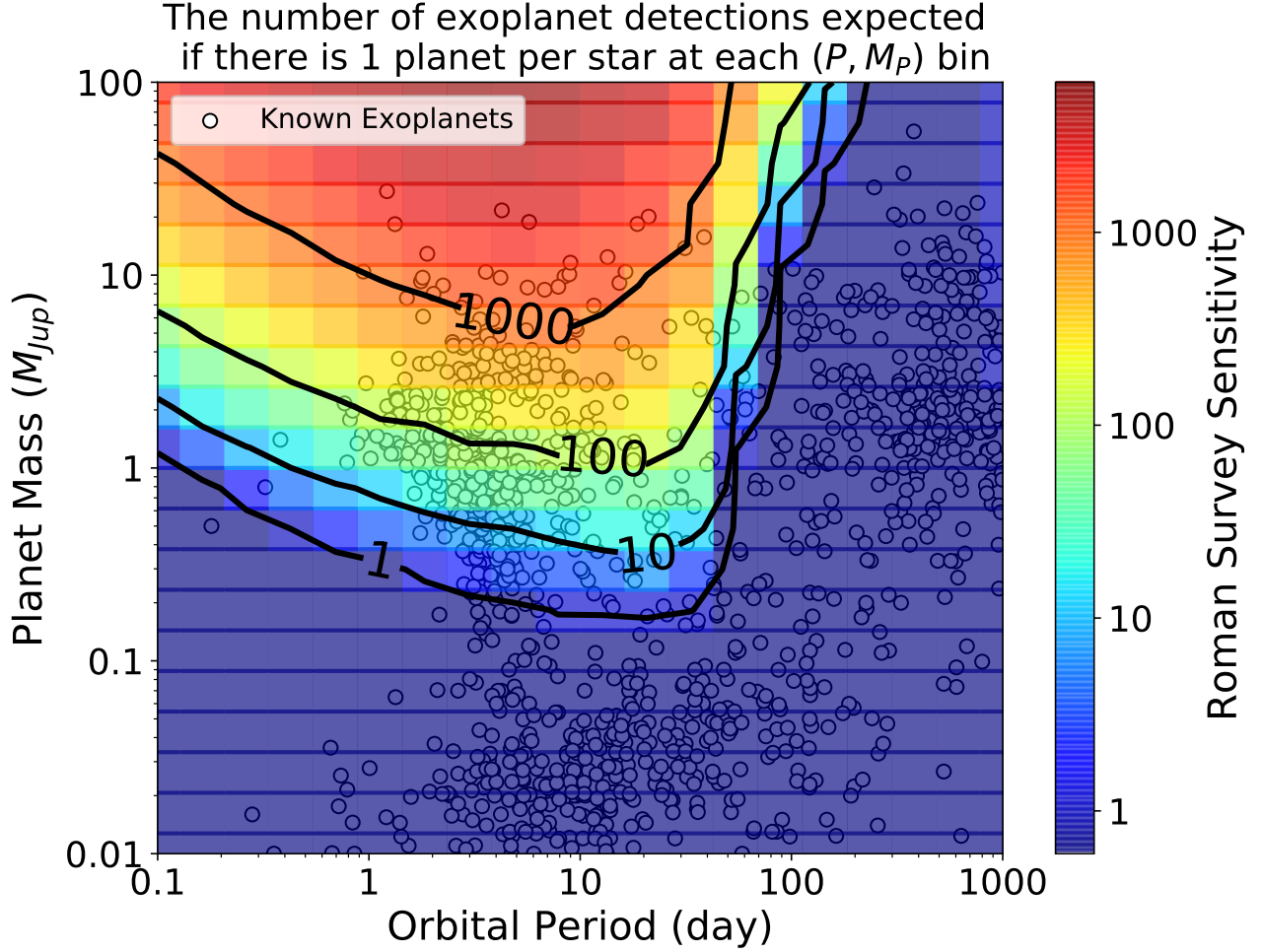


Figure 6. *Roman* xallarap sensitivity in the mass-orbital period plane. The color map shows the number of detections for xallarap planets or brown dwarfs during the *Roman* mission at a given mass and orbital period grid if there is one planet per star at a given grid. The open circles represent confirmed exoplanets referenced from [NASA Exoplanet Archive](#) (Akeson et al. 2013).

resent the distributions of σ_{M_P}/M_P and the black lines correspond to contour lines of our detection threshold of $(\sigma_{M_P}/M_P) = 0.3$. The row and column of a panel correspond to the labeled values of u_0 and t_E . For example, in the case of $\log(t_E) = 2$, $\log(u_0) = -1.5$ (bottom right panel), the *Roman* light curve has a potential to precisely measure the mass of a warm Jupiter with an orbital period of 10-30 days via xallarap. We found that M_P is well constrained when t_E is longer and u_0 is smaller in a given (M_P, P_ξ) grid. One also can find that there are sharp cut-offs of the sensitivity with the orbital period of a few dozens of days. This might be because the *Roman* observing window of 72 days could not cover the full orbital period of the events beyond the cut-off and

thus is insufficient to constrain the xallarap parameters⁴. This can be expected from the results of Figure 3 and 4.

3. PREDICTION OF THE YIELDS OF CLOSE-IN EXOPLANETS WITH XALLARAP

3.1. Simulating on the *Roman* Observation

In this section, we estimate the detection number of close-in planets and brown dwarfs (BDs) in source systems via xallarap during the *Roman* mission. To simulate the *Roman* microlensing survey, we employ the sin-

⁴ When we derive the sensitivity maps, we consider only an observing window of a single season. The sensitivity might extend toward the longer orbital period if we consider all the observing windows. However, it is not expected to be so much because of the results of Figure 4 and because there are long time-gaps between the *Roman* observing windows. Here we focus on only short-period planets and brown dwarfs.

Table 1. Parameters for *Roman* Galactic Exoplanet Survey

Survey Area	1.97 deg ²
Mission Baseline	4.5 years
Seasons	6 × 72 days
Observation Fields	7
Microlensing Events with $ u_0 < 1$	~ 27000
<i>W146</i> Exposures	~ 41,000 per fields
<i>W146</i> Cadence	15 minutes
Photometric Precision	~0.01 mag @ <i>W146</i> ~ 21.15

NOTE— The parameters for the Cycle 7 design we use are fully described in Penny et al. (2019) and Johnson et al. (2020). In this paper, we do not consider any observations with the Z087 filter and other filters that are to be conducted during the *Roman* microlensing survey, which could improve our prediction of planet yields to some extent.

gle stellar lens module of the GULLS microlensing simulator (Penny et al. 2013, 2019) which uses version 1106 of the Besançon Galactic population synthesis model (Robin et al. 2003, 2012) to generate pairs of lens and source stars. In Table 1, we summarize the survey parameters for the Cycle 7 design that we use in our simulation. The full survey details are described in P19 and Johnson et al. (2020). Note that we consider only single-lens events whose peaks are within the *Roman* observing window.

We classified the simulated *Roman* events from GULLS by the values of $(u_0, t_E, W146_S)$ into bin $7 \times 10 \times 10$ over the ranges of $14 < W146_S < 28$ mag, $-2 < \log u_0 < 0$, and $0 < \log(t_E/\text{day}) < 2.5$, respectively. We generated the sensitivity maps with the parameters at the center of each bin to be used for all events in each bin. Then we counted the number of detected events by using the corresponding sensitivity maps at each (M_P, P_ξ) grid. Figure 6 shows the resultant detections, i.e., the expected planet yields during the *Roman* survey mission if all source stars were to have a planet at each (M_P, P_ξ) grid point. The black solid lines represent the contours of the planet yields for 1, 10, 100 and 1000. The detection sensitivity peaks around $P_\xi = 20 \sim 30$ days and there it reaches to sub-Jovian or Saturn masses. In Figure 6, we also plotted observed exoplanets (open dots) from the NASA Exoplanet Archive (Akeson et al. 2013). *Roman*’s sensitivity to planets via the xallarap effect largely covers the parameter spaces of hot and warm Jupiters with $M_P > 0.5 M_{\text{Jup}}$ and $0.1 < P < 100$ days, which suggests that this method could be useful to probe the hot and warm Jupiter populations in the Galactic bulge.

Note that we used only a single 72 days season for each event.

3.2. Planet Yields

In order to estimate the planet yields, we assume the secondary mass and period distributions. We describe the distribution function f as a double power law,

$$\frac{\partial^2 f}{\partial \ln M \partial \ln P} = C_{\text{norm}} \left(\frac{M_P}{M_{\text{Jup}}} \right)^{\alpha_M} \left(\frac{P}{\text{day}} \right)^{\beta_P}, \quad (17)$$

where C_{norm} is a normalization factor. In this work, we adopted the power law indexes of $\alpha_M = -0.31 \pm 0.2$ and $\beta_P = 0.26 \pm 0.1$ derived by Cumming et al. 2008, (hereafter C08). These values are derived by using 48 RV-detected planets ranging $0.3 < M_P < 10 M_{\text{Jup}}$ and $2 < P < 2000$ days that are around Sun-like stars. We adopted $C_{\text{norm}} = 0.036 \text{ dex}^{-2} \text{star}^{-1}$ to be consistent with a planet frequency of 10.5% around Sun-like stars in these ranges derived by C08. Note that we simply extrapolate this C08’s power-law to the ranges $0.01 < M_P < 100 M_{\text{Jup}}$ and $0.1 < P < 1000$ days because it is still uncertain. The extrapolation below $0.3 M_{\text{Jup}}$ hardly affects the final result because the sensitivities to low-mass planets with $< 0.3 M_{\text{Jup}}$ is very low and the *Kepler* survey suggested that the occurrence rate does not significantly rise until below Neptune size of $\sim 5 M_\oplus$ (e.g. Fressin et al. 2013). The extrapolations to other range need cautions as discussed below. We also estimate the yields assuming a simple frequency model of $(\alpha_M, \beta_P) = (0, 0)$ and $C_{\text{norm}} = 0.208 \text{ dex}^{-2} \text{star}^{-1}$, which corresponds to single planet per star over the ranges. This can be considered as the reference yields.

Figure 7 represents the expected yields of the *Roman* observations assuming the extended C08 distribution. The three left panels show the distributions of t_E , u_0 , and $W146_S$ for events in which the planet/BD companion around the source is detected. The yields are expected to largely come from the events with $18 < W146_S < 22$ mag, which mostly consists of main sequence source stars. Note that although the histogram with u_0 indicates that the detections increase towards larger u_0 , as shown in Figure 5, the events with large u_0 are only sensitive to massive companions. The right panel in Figure 7 shows the distribution for the number of planets and BDs detections over the parameter spaces of masses and periods assuming the frequency from C08. Table 2 summarizes the expected yields with assuming the two different distribution functions. Adopting the extended C08 distribution, we found that ~ 10 planets with $M \leq 10 M_{\text{Jup}}$ would be detected by xallarap. We can expect ~ 30 companions with $10 < M_P < 100 M_{\text{Jup}}$ if the extrapolation of C08 is correct. However, due to

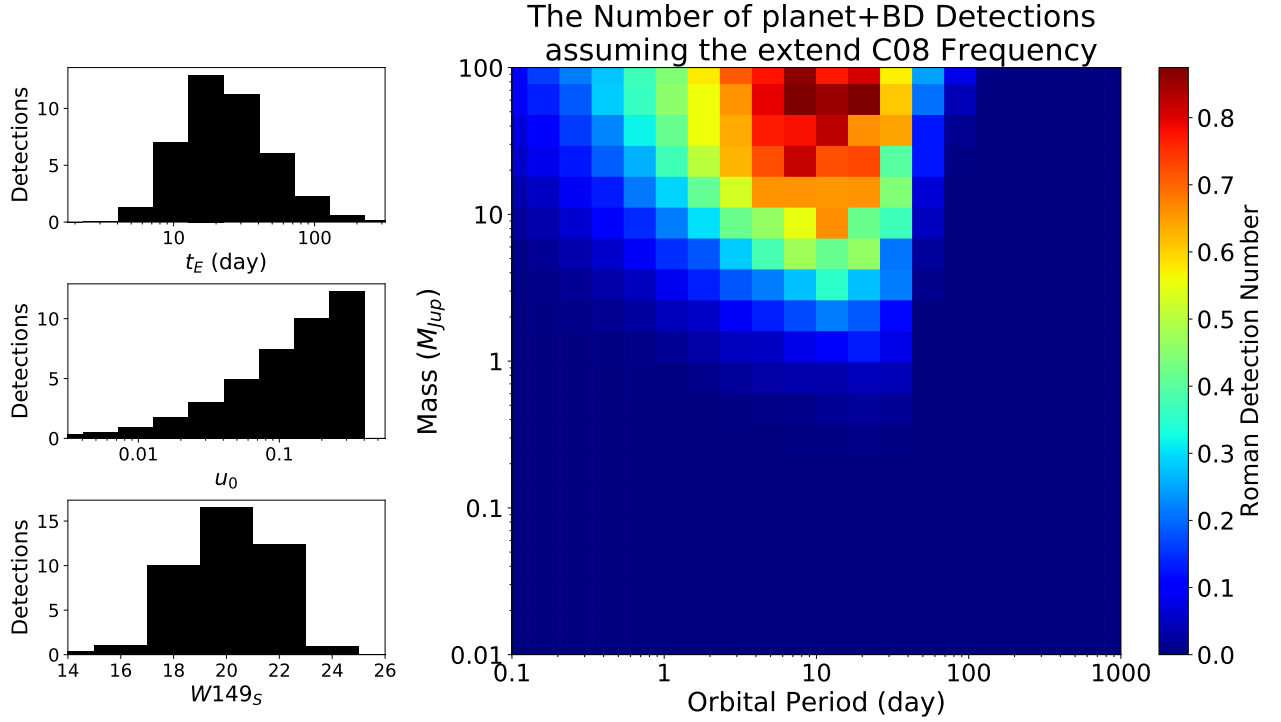


Figure 7. Expected number of the planet and brown dwarf yields during the *Roman* mission assuming the extended C08 frequency. The left three panels are the histograms of the yields binned by t_E , u_0 , and $W149_s$. The color map in the right panel represents the yields per a given mass-orbital period grid.

Table 2. Expected Yields

	Distribution Function	
	Simple Model ^a	Extend C08 ^b
Companion Mass M_P (M_{Jup})		
$10 \leq M_P < 100$	409.6	30.9
$1 \leq M_P < 10$	63.3	10.1
$0.1 \leq M_P < 1$	1.05	0.37
$M_P < 0.1$	0.0022	0.0014
Orbital Period P (days)		
$100 \leq P < 1000$	0.043	0.007
$10 \leq P < 100$	112	15.7
$1 \leq P < 10$	243	20.7
$P < 1$	118	5.1
Total	474	42

^aSimple power-law function with $(\alpha_M, \beta_P) = (0, 0)$.

^bCumming et al. (2008) power-law function extended over ranges of $0.01 < M_P < 100 M_{Jup}$ and $0.1 < P < 1000$ days.

“brown dwarf desert” (Grether & Lineweaver 2006), BD discoveries may be much less common than predicted us-

ing the C08 frequencies⁵. We can test the “brown dwarf desert” in the Galactic bulge by applying this method to the upcoming *Roman* light curves.

4. DISCUSSION

4.1. How to Distinguish Lens Orbital Motion

If the lensing body is in a binary system, lens orbital motion (LOM) will provide a similar effect to that of xallarap, which has been pointed out in several papers (Rahvar & Dominik 2009; Penny et al. 2011). In a planetary system with orbital period of $P \leq 30$ days, a projected angular separation between a lensing host star and its planet in units of θ_E , $s = a/\theta_E$, is expected to be an order of $s \leq 0.06$. It is unlikely that a lens companion with such a small s provides noticeable light curve deviations by their extremely small caustics. For example, Penny et al. (2011) found that periodic (caustic) features of light curve due to LOM would be most detectable for binary-lens with semimajor axes of ~ 1 au. Thus it is difficult to distinguish between xallarap and

⁵ Under the extend C08 function, the existence frequency of BDs around solar-type star is $\sim 3\%$ per star. Grether & Lineweaver (2006) reported that is $< 1\%$ per star. More recently, Santerne et al. (2016) reported the occurrence rate of BDs within 200 days of the orbital period with $0.29 \pm 0.17\%$ in the *Kepler* transit candidates.

LOM. However the degeneracy may be resolved when following additional high-order effects are observed in the light curves. The following effects can be observed only in the xallarap events, not in the LOM events.

Magnified Planet Flux: Planets orbiting source stars produce reflect light from their host and/or emit their own flux from thermal emission. If flux from these companions are magnified, we can observe these contributions in the light curve, as a so-called binary source microlensing event. (Graff & Gaudi 2000; Sajadian & Rahvar 2010). Typical flux ratios between solar-type stars and hot Jupiters in the *W146* band is on the order of $\sim 10^{-3}$ to 10^{-4} . Using this detection channel, Bagheri et al. (2019) estimated that *Roman* will discover ~ 70 exoplanets from single-lens events and ~ 3 exoplanets from binary-lens events.⁶ We expect that the binary source effect might be observed in the *Roman* xallarap single-lens events of $P < 5$ days, which corresponds to $\sim 50\%$ of the total yields. It would also help us to constrain the orbital parameters of source systems because it provides the geometric relation between host and planet at the time when the planet is magnified. Full binary-source modeling including xallarap effect (Miyazaki et al. 2020) is more realistic and might have more sensitivity, but this is out of the scope of this work.

Transiting Source Stars: If the planet transits the source star, we can also simultaneously observe the transiting signal during the microlensing event (Lewis 2001; Rybicki & Wyrzykowski 2014). Typical amplitudes of the transit signal for Jupiter-size planet would be $\sim 1\%$ of the source brightness, which will be easily detectable for most xallarap planetary events. For example, *Roman* is expected to detect thousands on transiting hot Jupiters, including in the galactic bulge (McDonald et al. 2014; Montet et al. 2017). The geometric transit probability of warm Jupiters is $\sim 5\%$ so that $\sim 5\%$ of xallarap planetary events could be distinguishable from LOM events by the transit signals. With the measurement of the planet radius by the transit, we can estimate the density of the planet in the combination with the mass measurement by xallarap. And, this potentially can test how chemistry affects giant planet structures (e.g. Cabral et al. 2019).

⁶ Note that their most detection samples were composed of hot Jupiters with $a < 0.05$ au, and they assumed a source star has an exoplanet per event.

Ellipsoidal Variations: Ellipsoidal variations can be caused by tidal effects on the source from the companion (Morris 1985). The amplitude of the ellipsoidal variation is approximated by

$$\begin{aligned} A_{\text{ellip}} &\simeq \alpha_{\text{ellip}} \frac{M_P \sin \lambda_\xi}{M_S} \left(\frac{R_S}{a_{SC}} \right)^3 \sin \lambda_\xi \\ &= 13 \text{ ppm} \left(\frac{M_P \sin \lambda_\xi}{M_{\text{Jup}}} \right) \left(\frac{R_S}{R_\odot} \right)^3 \\ &\quad \times \left(\frac{M_S}{M_\odot} \right)^{-2} \left(\frac{P_\xi}{\text{day}} \right)^{-2} \alpha_{\text{ellip}} \sin \lambda_\xi, \end{aligned} \quad (18)$$

where R_S is the radius of the source star. The coefficient α_{ellip} accounts for the stellar limb darkening and gravity darkening:

$$\alpha_{\text{ellip}} = 0.15 \frac{(15 + u)(1 + g)}{3 - u}, \quad (19)$$

where g and u are the coefficients of the gravity darkening and linear limb darkening, respectively (Shporer 2017). It would be difficult to observe this effect for the xallarap planetary events. However, it might be possible for events of substellar source companions.

Doppler Beaming: It is known that a line of sight motion due to the orbit causes a periodic variation in the light curve, also known as Doppler beaming (Loeb & Gaudi 2003; Shporer 2017). The photometric amplitude of the beaming effect A_{beam} is described as below,

$$\begin{aligned} A_{\text{beam}} &= 2.8 \times 10^{-3} \alpha_{\text{beam}} \left(\frac{P_\xi}{\text{day}} \right)^{-1/3} \\ &\quad \times \left(\frac{M_S + M_P}{M_\odot} \right)^{-2/3} \left(\frac{M_P \sin \lambda_\xi}{M_\odot} \right), \end{aligned} \quad (20)$$

where α_{beam} is the coefficient accounting of variation of photon amounts in a specific band, e.g. $\alpha_{\text{beam}} \equiv 1$ in bolometric light. For longer orbital period of $P_\xi > 10$ days, the amplitude of this effect is much stronger than that of the ellipsoidal variations and it is more promising to observe.

These effects may be able to resolve the degeneracy between the xallarap and LOM interpretations in some fraction of xallarap events and provide additional information for source systems.

4.2. Short-period Populations in the Galactic Bulge Revealed by *Roman*

Some observational results have suggested that there are possible differences in planetary populations between

the local neighborhood and the distant region of our Milky Way. RV surveys around the local region close to the Sun indicates an occurrence rate of hot Jupiters of order 1% (Cumming et al. 2008). On the other hand, *Kepler* transit survey toward the Cygnus region suggested the occurrence rate of $0.4 \pm 0.1\%$ (Howard et al. 2012), which is approximately half of that in the local neighborhood. Penny et al. (2016) used a sample of 31 microlensing exoplanetary systems and suggested the abundance of planets might be less in the Galactic bulge than the disk. Such studies would be very important to help understanding whether the planetary formations could depend on its surrounding environment in our Galaxy.

Montet et al. (2017) predicted that *Roman* is expected to discover $\sim 100,000$ transiting planets and enable us to directly confirm several thousands hot Jupiters via its secondary eclipses in the light curves. A large fraction of the transiting planets will belong to the Galactic bulge. However, in general, the most of host stars are too faint to conduct follow-up RV observations for constraining their planetary mass and avoiding false positives. Mon-

tet et al. (2017) also suggested some feasibilities for the validation for transiting planets and the estimation of their masses by using phase curve variations although it requires high photometric precisions to observe. Applying our xallarap method to the *Roman* microlensing light curves, we can expect to discover some dozens of hot and warm Jupiters and close-in BDs with measured masses. These samples will help our understanding of the exoplanet demographics at short orbital periods in the Galactic bulge. For larger masses, they are also useful to probe the “brown dwarf desert” around main-sequence stars and study of stellar binary distribution in the Galactic bulge.

Software: `numpy` (vanderWalt et al. 2011), `matplotlib` (Hunter 2007)

We would appreciate B. Scott Gaudi, Daisuke Suzuki, Kento Masuda, Akihiko Fukui, Yuki Hirao, Iona Kondo, and Clément Ranc for valuable comments and discussions.

APPENDIX

A. $\Delta\chi^2$ THRESHOLD AND FISHER MATRIX ANALYSIS

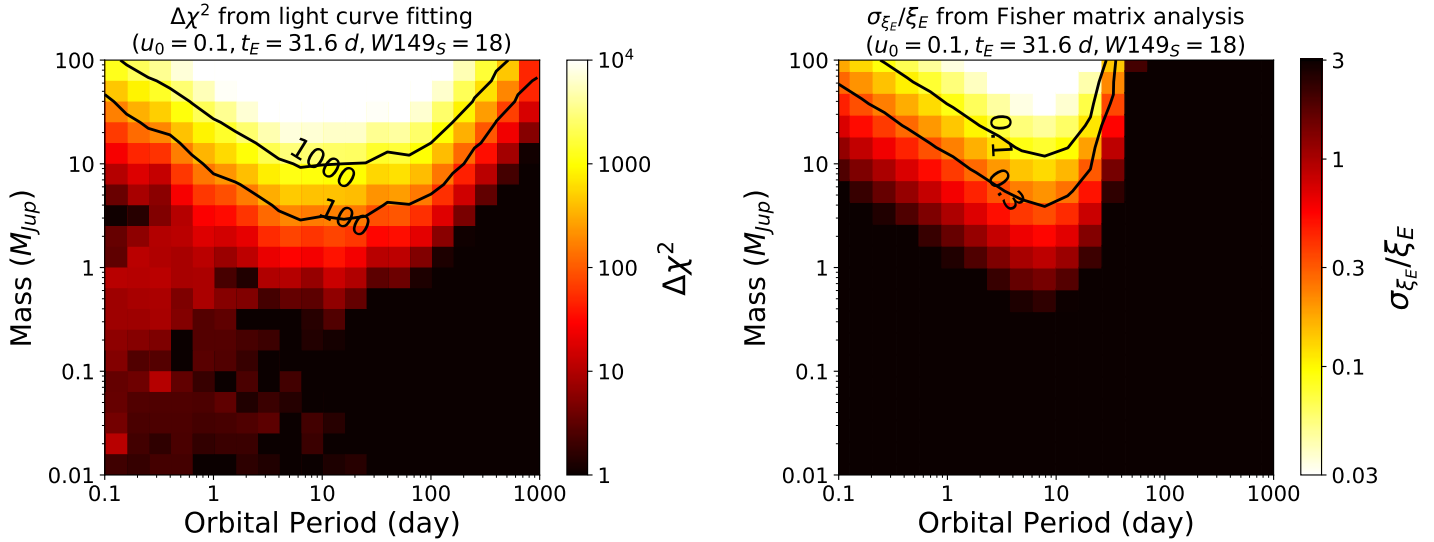


Figure 8. The comparison of distributions over the mass-period diagram between $\Delta\chi^2$ from the light curve fitting (left panel) and the parameter uncertainty from the Fisher matrix analysis (right panel).

$\Delta\chi^2$ has been often chosen as a detection threshold of planets in most microlensing simulations (e.g. Bennett & Rhie 1996; Penny et al. 2019; Johnson et al. 2020) possibly because quantifying the detectability can not be analytically solved for binary-lens modeling (see Penny et al. 2011 for a discussion of the challenges). Rahvar & Dominik (2009) studied xallarap induced by planetary companions also adopted the $\Delta\chi^2$ threshold of 11.07 for the detection threshold of planets. However, we adopt the Fisher matrix analysis that allows us to quantify the ability not only detecting

xallarap signals but also characterizing the physical parameters. For demonstrating this, we conduct both the Fisher matrix analysis and light curve fitting in the same condition and compare them.

Figure 8 represents an example of the result with a simulated *Roman* event of $(u_0, t_E, W146_S) = (0.1, 31.6 \text{ days}, 18)$. In the left panel, the $\Delta\chi^2$ distribution is shown as a color map over the mass-period diagram. Here $\Delta\chi^2 = \chi_{\text{xallarap}}^2 - \chi_{\text{standard}}^2$ and χ_i^2 value are calculated fitting each model to the simulated light curve. The right panel shows the uncertainty of xallarap amplitude ξ_E estimated from the Fisher matrix analysis. In the parameter space of $(P_\xi \geq 40 \text{ day}, M_P \geq 1 M_{\text{Jup}})$, one finds it is not possible to constrain ξ_E well though there should be large $\Delta\chi^2$ improvements if we fit the light curve by xallarap model. This can be because the light curve is strongly affected by only the source acceleration of a single direction and thus only one component of the xallarap vector ξ_E can be constrained. For constraining xallarap parameters, it would be required to observe the source accelerations during the full time of source orbits. However, we note that it might be possible that the periodogram analysis of the residuals from a standard single-lens fit can constrain the orbital period of the planet sufficiently to enable an estimate of the planet mass (Nucita et al. 2014; Giordano et al. 2017).

B. UNCERTAINTIES ON D_S , θ_E , AND M_S

The ability of *Roman* to measure θ_E and D_S has been studied in several papers. It is expected that most *Roman* events will have their relative lens-source proper motion μ_{rel} measured via direct detection of lens light in the *Roman* images, which enables us to measure θ_E (Bennett et al. 2010, 2020; P19; Terry et al. 2020). Bhattacharya et al. (2018) estimated that *Roman* will measure the lens-source separations with less than 10% precision for most events. On the other hand, Gould & Yee (2014) analytically showed that events with photometric precisions of $\leq 0.01 \text{ mag}$ have chances to provide the measurements of θ_E with $\leq 10\%$ precision via astrometric microlensing in space-based microlensing experiments.⁷ D_S for bright source events can potentially be measured by the direct parallax (astrometry) measurements in the *Roman* survey data (Gould et al. 2015). Even if not for bright source events, the combination of the three measurements of the microlens parallax π_E , lens flux F_L , and θ_E allows us to directly determine D_S . Moreover, D_S can be statistically estimated with $\sim 20\%$ precision using priors of standard Galactic model (e.g. Sumi et al. 2011; Bennett et al. 2014). For main sequence stars, M_S is expected to be approximately estimated from the source magnitude and color which are obtained by the multi-band *Roman* photometry (we expect it with less than 20% precision using a stellar isochrone model, e.g., Bressan et al. 2012), and it will become more accurate if D_S is also measured. For evolved source stars, the mass can be constrained via the age distribution of the bulge. In this paper, we evaluate the *Roman* ability to characterize the physical parameters of the xallarap companions by adopting (σ_{M_P}/M_P) in Equation (16). Of course, the resultant errors on the companion's masses will become somewhat larger than the 30% ($\sigma_{M_P}/M_P = 0.3$) due to errors on D_S , θ_E and M_S . However, we expect the mass measurements would be possible by *Roman* with less than 40% precision in most cases even if all the errors were included.

REFERENCES

- Akeson, R. L., Chen, X., Ciardi, D., et al. 2013, *PASP*, 125, 989
- Bachelet, E., Hinse, T. C., & Street, R. 2018, *AJ*, 155, 191
- Bagheri, F., Sajadian, S., & Rahvar, S. 2019, *MNRAS*, 490, 1581
- Bennett, D. P. & Rhie, S. H. 1996, *ApJ*, 472, 660
- Bennett, D. P., Bally, J., Bond, I., et al. 2003, *Proc. SPIE*, 141
- Bennett, D. P., Bond, I. A., Udalski, A., et al. 2008, *ApJ*, 684, 663
- Bennett, D. P., Anderson, J., Beaulieu, J.-P., et al. 2010, *arXiv:1012.4486*
- Bennett, D. P., Batista, V., Bond, I. A., et al. 2014, *ApJ*, 785, 155
- Bennett, D. P., Bhattacharya, A., Beaulieu, J.-P., et al. 2020, *AJ*, 159, 68
- Bhattacharya, A., Beaulieu, J.-P., Bennett, D. P., et al. 2018, *AJ*, 156, 289
- Bressan, A., Marigo, P., Girardi, L., et al. 2012, *MNRAS*, 427, 127. doi:10.1111/j.1365-2966.2012.21948.x
- Broomhall, A.-M., Chaplin, W. J., Davies, G. R., et al. 2009, *MNRAS*, 396, L100
- Cabral, N., Lagarde, N., Reyl  , C., et al. 2019, *A&A*, 622, A49
- Cumming, A., Butler, R. P., Marcy, G. W., et al. 2008, *PASP*, 120, 531
- Dawson, R. I., & Johnson, J. A. 2018, *ARA&A*, 56, 175

⁷ They also show that source companions with short orbital periods of $P \leq 1 \text{ yr}$ hardly affect the measurements of the astrometric signatures.

- Dominik, M. 1998, *A&A*, 329, 361
- Fressin, F., Torres, G., Charbonneau, D., et al. 2013, *ApJ*, 766, 81
- Gilliland, R. L., Chaplin, W. J., Jenkins, J. M., et al. 2015, *AJ*, 150, 133
- Giordano, M., Nucita, A. A., de Paolis, F., et al. 2017, *International Journal of Modern Physics D*, 26, 1741009
- Gould, A. 2004, *ApJ*, 606, 319
- Gould, A. 2013, *ApJL*, 763, L35
- Gould, A. & Yee, J. C. 2014, *ApJ*, 784, 64.
doi:10.1088/0004-637X/784/1/64
- Gould, A., Huber, D., Penny, M., et al. 2015, *Journal of Korean Astronomical Society*, 48, 93
- Graff, D. S. & Gaudi, B. S. 2000, *ApJL*, 538, L133
- Grether, D. & Lineweaver, C. H. 2006, *ApJ*, 640, 1051
- Griest, K., & Hu, W. 1992, *ApJ*, 397, 362
- Han, C., & Gould, A. 1997, *ApJ*, 480, 196
- Han, C. & Jeong, Y. 1998, *MNRAS*, 301, 231
- Hayashi, C., Nakazawa, K., & Nakagawa, Y. 1985, *Protostars and Planets II*, 1100
- Howard, A. W., Marcy, G. W., Bryson, S. T., et al. 2012, *ApJS*, 201, 15
- Hunter, J. D. 2007, *Computing in Science and Engineering*, 9, 90
- Johnson, S. A., Penny, M., Gaudi, B. S., et al. 2020, *AJ*, 160, 123
- Lewis, G. F. 2001, *A&A*, 380, 292.
doi:10.1051/0004-6361:20011446
- Loeb, A. & Gaudi, B. S. 2003, *ApJL*, 588, L117
- Mao, S., & Paczynski, B. 1991, *ApJL*, 374, L37
- Marcy, G., Butler, R. P., Fischer, D., et al. 2005, *Progress of Theoretical Physics Supplement*, 158, 24
- McDonald, I., Kerins, E., Penny, M., et al. 2014, *MNRAS*, 445, 4137
- Morris, S. L. 1985, *ApJ*, 295, 143
- Mayor, M., & Queloz, D. 1995, *Nature*, 378, 355
- Miyazaki, S., Sumi, T., Bennett, D. P., et al. 2020, *AJ*, 159, 76
- Mogavero, F., & Beaulieu, J. P. 2016, *A&A*, 585, A62
- Montet, B. T., Yee, J. C., & Penny, M. T. 2017, *PASP*, 129, 044401
- Nucita, A. A., Giordano, M., De Paolis, F., et al. 2014, *MNRAS*, 438, 2466
- Paczynski, B. 1986, *ApJ*, 304, 1
- Penny, M. T., Kerins, E., & Mao, S. 2011, *MNRAS*, 417, 2216
- Penny, M. T., Kerins, E., Rattenbury, N., et al. 2013, *MNRAS*, 434, 2
- Penny, M. T., Henderson, C. B., & Clanton, C. 2016, *ApJ*, 830, 150
- Penny, M. T., Gaudi, B. S., Kerins, E., et al. 2019, *ApJS*, 241, 3
- Poindexter, S., Afonso, C., Bennett, D. P., et al. 2005, *ApJ*, 633, 914
- Rahvar, S., & Dominik, M. 2009, *MNRAS*, 392, 1193
- Robin, A. C., Reyl  , C., Derri  re, S., et al. 2003, *A&A*, 409, 523. doi:10.1051/0004-6361:20031117
- Robin, A. C., Marshall, D. J., Schultheis, M., et al. 2012, *A&A*, 538, A106. doi:10.1051/0004-6361/201116512
- Rybicki, K. & Wyrzykowski, L. 2014, *AcA*, 64, 65
- Santerne, A., Moutou, C., Tsantaki, M., et al. 2016, *A&A*, 587, A64
- Sajadian, S. & Rahvar, S. 2010, *MNRAS*, 407, 373
- Sumi, T., Bennett, D. P., Bond, I. A., et al. 2010, *ApJ*, 710, 1641
- Sumi, T., Kamiya, K., Bennett, D. P., et al. 2011, *Nature*, 473, 349
- Sumi, T., Udalski, A., Bennett, D. P., et al. 2016, *ApJ*, 825, 112
- Shporer, A. 2017, *PASP*, 129, 072001
- Spergel, D., Gehrels, N., Baltay, C., et al. 2015, *arXiv:1503.03757*
- Terry, S. K., Bhattacharya, A., Bennett, D. P., et al. 2020, *arXiv:2009.08461*
- van der Walt, S., Colbert, S. C., & Varoquaux, G. 2011, *Computing in Science and Engineering*, 13, 22
- Witt, H. J. & Mao, S. 1994, *ApJ*, 430, 505
- Wright, J. T., Marcy, G. W., Howard, A. W., et al. 2012, *ApJ*, 753, 160
- Zhu, W. & Gould, A. 2016, *Journal of Korean Astronomical Society*, 49, 93